Research Article

Formation of SS316L Single Tracks in Micro Selective Laser Melting: Surface, Geometry, and Defects

Zhiheng Hu, Balasubramanian Nagarajan, Xu Song, Rui Huang, Wei Zhai, and Jun Wei [ID]

Singapore Institute of Manufacturing Technology (SIMTech), Agency for Science, Technology and Research (A∗STAR),
73 Nanyang Drive, Singapore 637662

Correspondence should be addressed to Jun Wei; jwei@simtech.a-star.edu.sg

To fabricate complex parts with a fine resolution and smooth finish, micro selective laser melting (SLM) has been developed recently by combining three attributes: small laser beam spot, fine powder size, and thin layer thickness. This paper studies the effect of the micro-SLM process parameters on the single track formation of 316L stainless steel. The surface morphology, geometrical features, and defects have been analyzed in detail. The results highlight that laser power and scanning velocity have a significant effect on the formation of single tracks. The single tracks fabricated through micro-SLM with varying process parameters are classified into four types: no melting, discontinuous, continuous but unstable, and continuous tracks. Besides, the top surface of the tracks is observed with "double-crest" morphology, due to the high recoil pressure gradient generated by the extremely fine spot size. In addition, molten pool geometry (width, depth, and height) has been characterized to study the mode of the molten pool in micro-SLM. Finally, the occurrence of two typical defects within the tracks, keyhole pore and cavity at the edges, has been studied.

1. Introduction

Additive manufacturing (AM) processes manufacture the three-dimensional (3D) parts layer by layer according to a digital model and have a significant development in the past two decades [1]. Currently, AM of metals is focused mainly on the fabrication of components in macroscales. Due to the evergrowing demand for miniaturization, there is an increasing focus on fabricating microscale and nanoscale features using AM [2]. In comparison with the traditional metallic microfabrication techniques such as machining and forming [3], AM satisfies the demand for the fabrication of microparts with high geometrical complexity.

Selective laser melting (SLM) is one of the common AM technologies which utilize a high-intensity laser beam to selectively melt the metallic powders [4]. Typically, SLM systems use the laser beam size of tens to hundreds of microns [5, 6], powder size of 20–50 μm, and the layer thickness ranging between 20 μm and 100 μm. Since these

parameters significantly influence the part resolution, SLM has limitations towards microfabrication. In order to scale down the conventional SLM to increase the resolution suitable for micro-SLM, it is necessary to reduce the laser spot size, powder size, and layer thickness [7].

In SLM, fabricating a complex 3D part with the required properties is achievable through a multitude of well-fabricated single tracks. Since single track is the basic unit of the 3D parts, the formation of single tracks in conventional SLM and the underlying mechanism have been studied by various researchers. Yadroitsev et al. [8] fabricated 316L stainless steel single track samples and studied the relationship between the process parameters and the geometry using the ANOVA method. Yang et al. [9] estimated the condition of different molten pool modes of SLMed Ti-6Al-4V single track samples. Nie et al. [10] investigated the relationship between the process parameters and the geometry as well as the surface topography of the SLMed Al-Cu-Mg single track samples. Xiang et al. [11] explored the

defect forming mechanism of Ti-6Al-4V single tracks by the discrete element method. All the abovementioned research studies highlight that the process parameters including laser power, scanning velocity, and layer thickness have a significant effect on the formability, geometry, surface topography, and defects of the single tracks in SLM. In terms of process behavior, micro-SLM is expected to be different from the conventional SLM due to the finer laser beam size, layer thickness, and powder size. Therefore, in order to comprehend the micro-SLM process mechanisms, understanding the single track formation is essential.

Nevertheless, current research studies on micro-SLM are mainly concentrated on surface quality and geometry [12, 13]. To the best of our knowledge, there are hardly any research works on the process behavior and the underlying mechanisms during micro-SLM. Therefore, this paper is focused on the influences of the process parameters on the surface, geometry, and defects of the single tracks fabricated by micro-SLM. 316L stainless steel (SS316L) has been chosen as the material for the study. The underlying process mechanisms in the formation of single tracks during micro-SLM have been proposed.

2. Experimental Details

2.1. Materials. Gas-atomized SS316L powders was used in this experiment. The range of particle size of the powders was 5 to 22.49 μm with an average diameter of 13.32 μm. The scanning electron microscopy (SEM) image of the powder (Figure 1(a)) shows that it is almost spherical in shape. The chemical composition of the initial powder is shown in Table 1. Figure 1(b) is the cross-sectional optical microscopy (OM) image of the powder which reveals that there is no defect inside the powder.

2.2. Micro-SLM Experiments. A self-developed micro-SLM machine was used for the experiments. The system consists of a continuous wave IPG fiber laser ($\lambda = 1.07$ μm) with the maximum power of 100 W, focused spot size of 15 μm, an automatic powder delivery system, a building platform with the precision of 1 μm, an enclosed process chamber for inert gas environment, and a computer system for the process control.

Single tracks with a length of 5 mm were fabricated using the parameters listed in Table 2. For every process parameters, six samples were fabricated. A SS316L substrate of cylindrical shape with the diameter of 120 mm was used for the experiments. The substrate was preheated to 353 K before the experiment. Besides, the powder was dried for 4 h at 353 K before the experiment.

2.3. Characterization. The surface morphology of the single tracks was characterized by OM (Olympus MX51) and SEM (JEOL IT300 LV). Alicona optical 3D noncontact metrology system was used to capture the 3D topography of the tracks. The surface roughness (Ra) of the track center along the laser scanning direction was measured. The mean roughness of at least three measurements has been reported in this manuscript. The samples were cross-sectioned using wire-cutting,

followed by mounting, grinding, and polishing. The samples were then etched using Marble's reagent (50 ml HCl, 50 ml H_2O, and 10 g $CuSO_4$). The cross-sectional morphologies of the single tracks were then characterized by OM and SEM. The quantitative characterization of the track geometry was performed by the software Analysis Pro, and the average of six data was used for the analysis.

3. Results and Discussion

3.1. Surface Morphology of the Single Tracks. Figure 2 shows the surface morphologies of the SS316L single tracks fabricated by micro-SLM. Both the laser power and scanning velocity have a significant effect on the formation of the single tracks. Figure 2 has been classified into four zones based on the morphology of the single track. In zone A, no track can be observed due to the combination of low laser power and high scanning velocity. Zone B is composed of tracks which are discontinuous. In SLM, the powder and a portion of the substrate melt during the laser irradiation. However, due to the lower laser power and the shorter laser radiation time in this zone, the volume of the molten pool is expected to be low. The shallow remelted depth will lead to a lack of bonding between the track and the substrate [14]. At the same time, the lifetime of the molten pool will be short in addition to a low fluid flow strength. As a result, there will be no sufficient time for the track to spread [15]. Due to the poor bonding with the substrate, short lifetime, and weak fluid flow behavior, the molten pool formed in zone B is discontinuous along with the occurrence of the balling phenomenon. In zone C, the continuous tracks can be observed but the ripples caused by the solidification are found to be unstable. With the increased laser power and the reduced scanning velocity in zone C compared to zone B, the absorbed energy is adequate for the track to be formed continuously. However, the instability of the molten pool leads to unstable ripples in this zone, as seen clearly from Figure 2. Insufficient fluid flow could make the track to undulate, causing poor surface quality of the formed tracks. When the laser power further increases and scanning velocity further decreases, the track observed is continuous and the ripple caused by the solidification is stable (zone D). In this zone, the lifetime of the molten pool is sufficient for a stable track to form. No macroflaw can be observed due to the sufficient energy absorbed by the powder bed.

Energy density is usually used to determine the morphology of the molten pool in SLM [16]. Figure 3 compares the occurrence of different surface morphologies with the same linear energy density (E_l, $E_l = P/V$) but varying laser power and scanning velocity. It can be clearly observed that the morphologies of the formed tracks under the same energy density are different. The track formation changes from discontinuity to continuity, indicating that the energy density may not be a good indicator of controlling the molten pool morphology in micro-SLM. This observation confirms that the conclusion obtained by Bertoli et al. [5] and Xiang et al. [17] for the conventional SLM is also applicable for micro-SLM process.
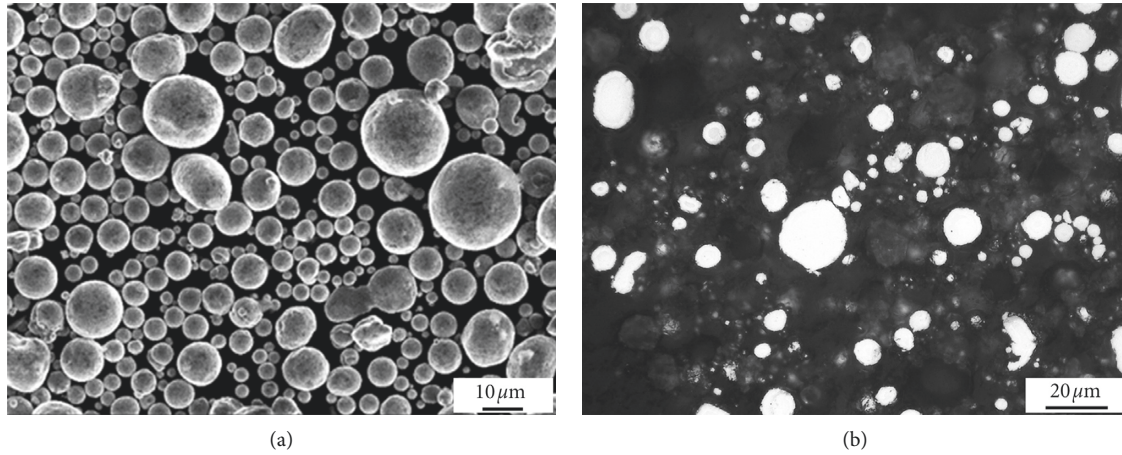
(a)

(b)

Figure 1: Morphology of 316L stainless steel powder. (a) SEM micrograph of the surface topography. (b) OM micrograph of the cross section.

Table 1: Chemical composition of the initial powder.

Element	Ni	Cr	Mo	Si	Mn	C	P	Cu	Fe
Wt. (%)	12.60	17.70	2.67	0.73	1.64	0.027	0.010	0.15	Bal.

Table 2: Process parameters used in the micro-SLM experiments.

Process parameters	Value
Laser power (P, W)	20, 30, 40, 50, 60, 70, 80, 90, 100
Scanning velocity (v, mm/s)	400, 800,1200, 1600, 2000, 2400, 2800
Layer thickness (μm)	10

3.2. Surface Roughness. Figure 4 compares the surface roughness (Ra) at the center of the single track fabricated under different process parameters. The effect of laser power on the Ra exhibits varying behaviors for the three scanning velocities. For a relatively low scanning velocity (400 mm/s), Ra dramatically decreases initially and then remains stable when the laser power increases within the chosen range. A correlation between Figures 4 and 2 reveals that the surface with a relatively higher Ra corresponds to either discontinuous (zone B) or continuous but unstable tracks (zone C). The poor surface finish typically signifies the instability of the single track. When the laser power increases, the lifetime of the molten pool becomes adequate for the liquid to spread, resulting in a smoother surface. Similarly, for a medium scanning velocity (1200 mm/s), the Ra decreases first with an increase in laser power from 50 W to 60 W. However, the roughness saturated before increasing again along with an increase in laser power between 70 W and 100 W. This difference in behavior with 1200 mm/s can be attributed to the reduction in the lifetime of the molten pool and the fluid flow strength while the scanning velocity increases from 400 mm/s to 1200 mm/s. If the fluid flow strength is insufficient to overcome the viscous drag, there will be inefficient spreading of the molten pool, followed by a formation of surface asperities [18]. When the laser power
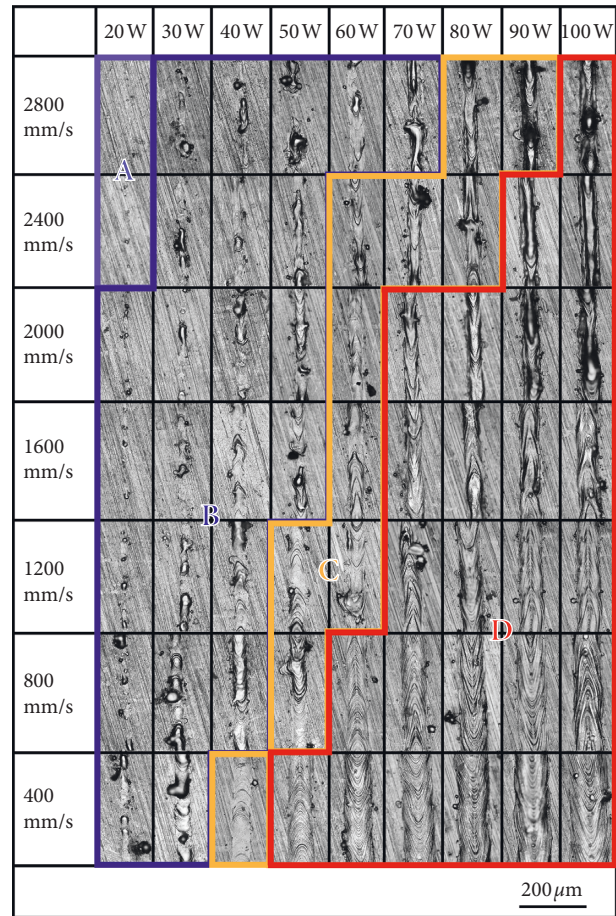

Figure 2: Surface morphologies of the single tracks fabricated by micro-SLM at different laser powers and scanning velocities (zone A: no melting; zone B: discontinuous; zone C: continuous but unstable; zone D: continuous stable).

increases, the melted powder volume increases, resulting in a greater demand for the flow driving forces and lifetime of the molten pool. Although the increased laser power increases the liquid flow driving forces and lifetime of the
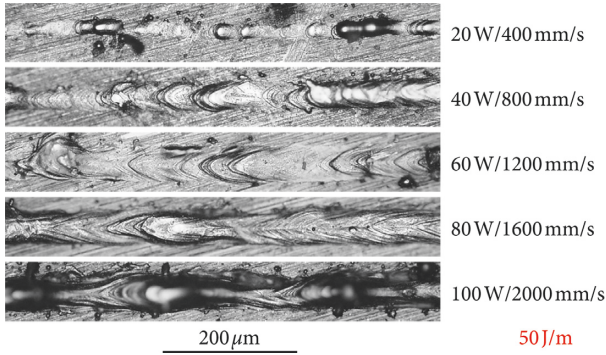
FIGURE 3: Surface morphologies of the single tracks at constant energy density (50 J/m).
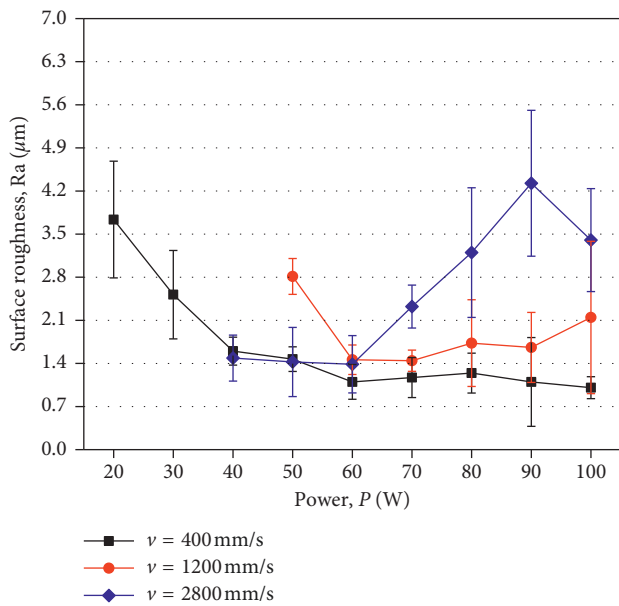

FIGURE 4: Surface roughness of the single tracks with changes in laser power and scanning velocity.

molten pool, they might fail to attain the required levels. Thus, when the laser power increases to 100 W, the fluid flow driving forces might not be enough for the molten pool spreading, which results in the increase in the Ra. For the much higher scanning velocity (2800 mm/s), the minimum Ra occurs between 40 and 60 W which then increases dramatically along with the laser power before reducing for 100 W. In the first stage (40–60 W), the amount of the melted powder is very little (Figure 2, close to zone A) so that the measured surface shows a relatively lower Ra. Due to the low temperature field, some amount of powders experiences only sintering instead of full melting. In the second stage (60–90 W), the track gradually becomes continuous from discontinuous (Figure 2, from zone B to zone C) leading to an increase in Ra. The final stage (90–100 W, from zone C to zone D) is similar to the downward trend for the samples fabricated at 400 mm/s. All the observations for surface roughness match with the

surface morphology as shown in Figure 2. From the results, it is noted that the best surface roughness (Ra) of the single track achieved has been 1 μm approximately.

3.3. Molten Pool Morphology. Figure 5 compares the SEM images of the surface morphologies of the single tracks fabricated at the scanning velocity of 400 mm/s. As described earlier, continuity and stability behavior of the tracks with the changes in laser power can be confirmed from Figure 5. Besides, it can be seen that there is a depression along the center at the molten pools for higher laser powers.

Figure 6 shows the OM images of the cross section of the sample fabricated by 50 W and 800 mm/s. It can be seen that the center of the molten pool is lower than its left and right side, highlighting two crests in the cross section. This "double-crest" surface is different from the molten pool morphologies typically observed in the conventional SLM. However, the "double-crest" surface commonly occurs in micro-SLM, as observed from Figures 5 and 6. Table 3 shows the occurrence of "double-crest" surface. For the analysis, all the samples fabricated with the scanning velocity of 400 mm/s, 800 mm/s, and 1200 mm/s as well as the laser power of 50 W and 60 W were included. This phenomenon is observed to take place when the laser power is high and the scanning velocity is low. The occurrence of "double-crest" surface can be explained through the interaction of molten pool with the recoil pressure. The recoil pressure (P_r) can be expressed according to the following equation [19]:

$$P_r = \frac{AB_0}{\sqrt{T_s}} \exp\left(-\frac{m_v L_v}{k_B T_s}\right), \tag{1}$$

where A is a numerical coefficient dependent on environmental pressure, B_0 is an evaporation constant, m_v is the mass of the molecule, L_v is the latent heat of the evaporation, k_B is the Boltzmann constant, and T_s is the surface temperature. It can be understood from equation (1) that the recoil pressure increases exponentially with the surface temperature increase. Because of the small beam size, the temperature gradient is expected to be high during the micro-SLM process, which hence leads to the high recoil pressure gradient. For a relatively moderate gradient, the recoil pressure will push the molten pool to spread uniformly. But, if the recoil pressure gradient is very high, more liquid will be pushed from the center to the near-center region rather than outward ejection. As a result, there will be liquid stacking. Before the solidification completes, the recoil pressure will push the liquid to the two sides. The crest forms after solidification. Due to the liquid stacking at the both sides, "double-crest" surface forms. As the recoil pressure grows exponentially as the surface temperature increases, this phenomenon is more likely to take place when the laser power is high and scanning velocity is low during micro-SLM process.

3.4. Molten Pool Geometry. The height (H), the width (W), and the depth (D) of the molten pool (Figure 7(a)) are
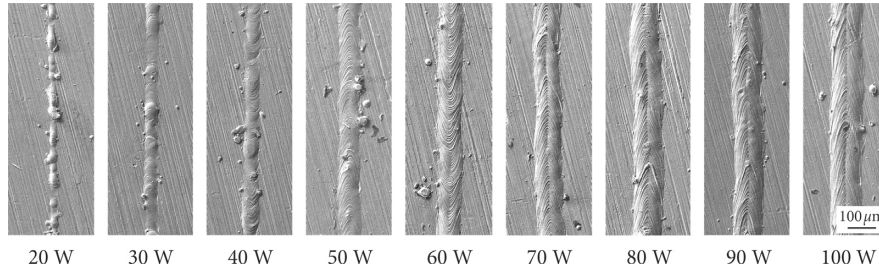
FIGURE 5: Comparison of SEM micrographs of single track morphologies at different laser powers ($v = 400$ mm/s).
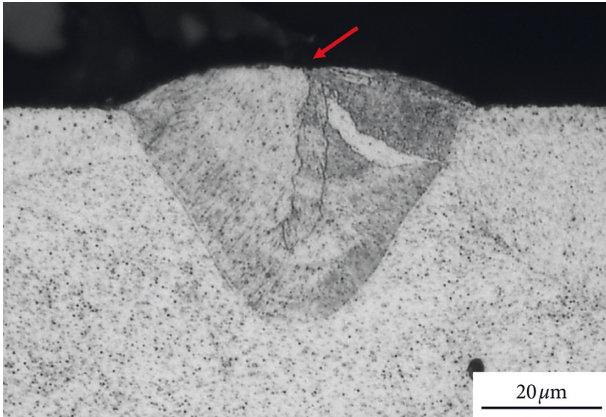

FIGURE 6: Cross section of the single track fabricated by micro-SLM ($P = 50$ W $v = 800$ mm/s).

TABLE 3: Occurrence of "double-crest" surface.

v (mm/s)	P (W)								
	20	30	40	50	60	70	80	90	100
400	✗	✗	✗	✓	✓	✓	✓	✓	✓
800				✓	✓				
1200	✗	✗	✗	✓	✓	✓	✓	✓	✓
1600				✓	✓				
2000				✓	✓				
2400				✗	✓				
2800	—	✗	✗	✗	✗	✗	✗	✗	✗

Note. —: no molten pool; ✗: "single-crest" molten pool; ✓: "double-crest" molten pool.

compared in Figures 7(b)–7(f). Figures 7(b)–7(d) illustrate the effect of laser power, whereas Figures 7(e) and 7(f) illustrate the effect of scanning velocity on the molten pool geometry. Generally, there is an upward trend of the molten pool width and depth when the laser power increases or the scanning velocity decreases. However, the height does not follow a monotonous trend with the changes in either laser power or scanning velocity. Similar to the conventional SLM, the process parameters directly determine the size of the molten pool in the micro-SLM process. With the increase in laser power and the reduction in scanning velocity, the energy absorbed by the powder bed increases, leading to a larger molten pool width and depth. In case of track height, two opposing effects play a role. After the laser radiation, the liquid formed can spill over to two sides and catch the neighboring particles and drag them into the molten pool,

hence creating denudation zone [20]. It was reported that the denudation zone increases along with the laser power [21]. So, it can be deduced that the ability of the liquid to drag powders into the molten pool becomes stronger when the energy absorbed increases, resulting in a taller track compared to the origin powder thickness. On the other hand, the fluid flow driving forces become stronger and the lifetime of the molten pool extends, which will drive the molten pool to spread, resulting in a reduced height. As a result of these two contrasting effects, no monotonous trend in track height could be observed when laser power or scanning velocity changes.

The molten pool mode, also as a geometric characteristic, is determined by the aspect ratio R (molten pool depth/laser spot diameter). The molten pool mode can be divided into two different modes: conductive mode with a small aspect ratio and keyhole mode with a rather large aspect ratio (i.e., $R > 1$) [22]. Table 4 summarizes the molten pool mode of the single tracks fabricated by different process parameters. It can be drawn that the keyhole mode usually takes place when the laser power is large and the scanning velocity is small. Figure 8 shows the SEM images of the cross section with different molten pool modes. The shape of the molten pool transforms from a V shape to an ellipse when the molten pool mode changes from the keyhole mode to conductive mode.

3.5. Single Track Defects. Figure 9 shows the typical defects of the single track. The keyhole pore (red arrow) can be identified from Figure 9(a), whereas the cavity at the molten pool edges (red arrow) is shown in Figure 9(b). Figure 8 also shows the evolution of the defects with changes in the scanning velocity. For the laser power of 60 W, the defect of the molten pool is the keyhole pore (Figure 8, red arrow, 400 mm/s) when scanning velocity is low. When the scanning velocity increases, the samples become defect-free (800 mm/s, 1200 mm/s, 1600 mm/s). When the scanning velocity further increases, the cavity at the molten pool edges (red arrows, 2000 mm/s and 2400 mm/s) takes place. Table 4 summarizes the defects. Keyhole pore takes place only in the keyhole-mode molten pool. When the laser power is high and the scanning velocity is low, keyhole-mode molten pool forms, where it is easy for the molten pool to entrap the gas. The pore forms after solidification as there is not enough time for the gas to escape. Keyhole pore usually occurs in a relatively deep location within the molten pool. The cavity
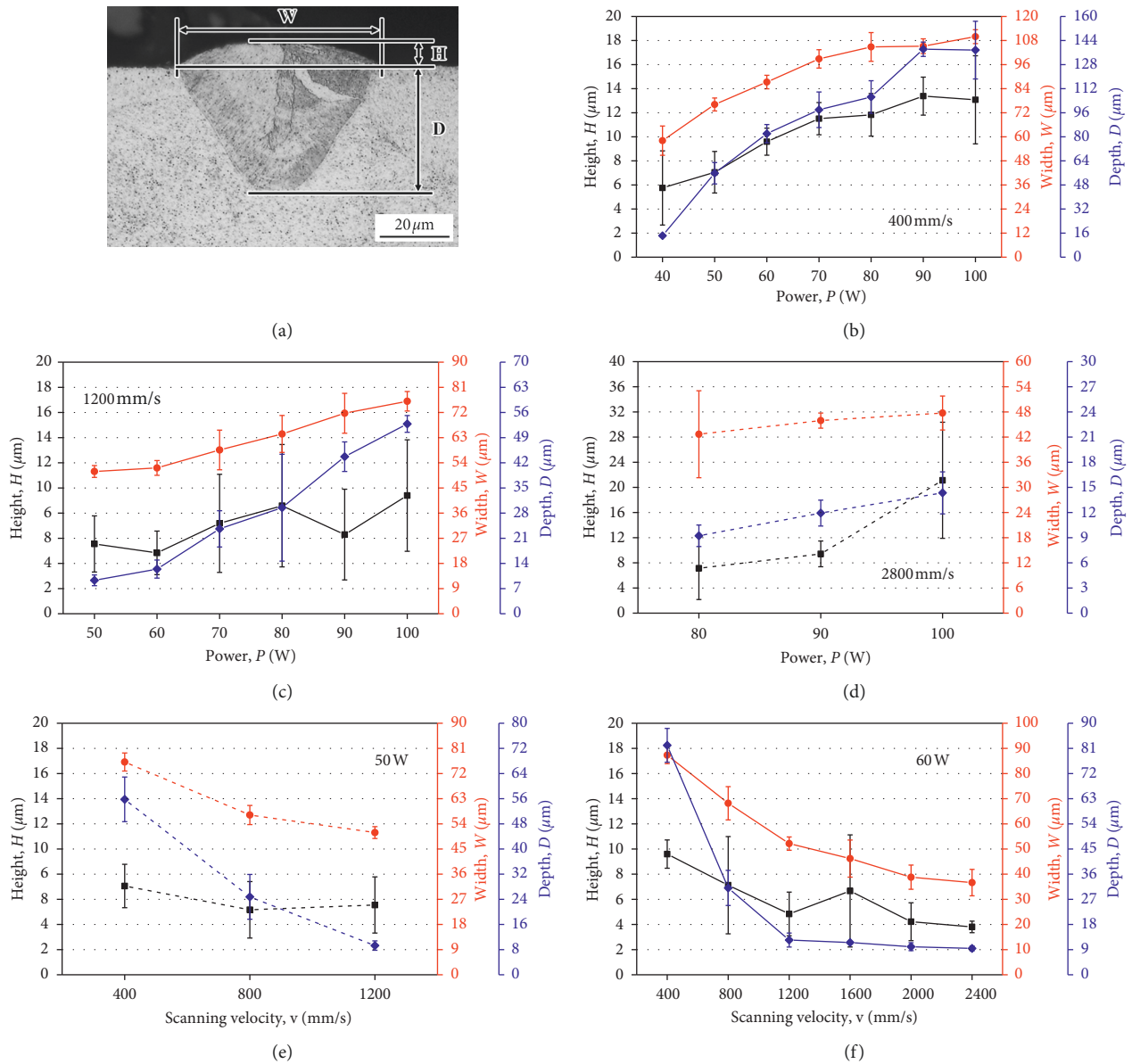
FIGURE 7: (a) Typical geometrical characteristics of the single track molten pool, (b–d) molten pool geometry versus laser power at different scanning velocities, and (e, f) molten pool geometry versus scanning velocity at different laser powers.

TABLE 4: Summary of molten pool mode/defects.

v (mm/s)	P (W)								
	20	30	40	50	60	70	80	90	100
400	—	—	C/✓	K/1	K/1	K/1	K/1	K/1	K/1
800				K/✓	K/✓				
1200	—	—	—	C/✓	C/✓	K/✓	K/1	K/1	K/1
1600				—	C/✓				
2000				—	C/2				
2400				—	C/2				
2800	—	—	—	—	—	—	C/2	C/2	C/2

Note. —: no molten pool/discontinuous molten pool; K: keyhole mode; C: conductive mode; ✓: no typical defects; 1: keyhole pore; 2: cavity at the edges.

defect occurs only when both the laser power and the scanning velocity are very high. For a higher laser power, it is easy for the molten pool to drag the liquid to the center. But, the short lifetime of the molten pool caused by the high scanning velocity leads to the lack of time for liquid spreading. So, the cavity forms after solidification. Figure 10
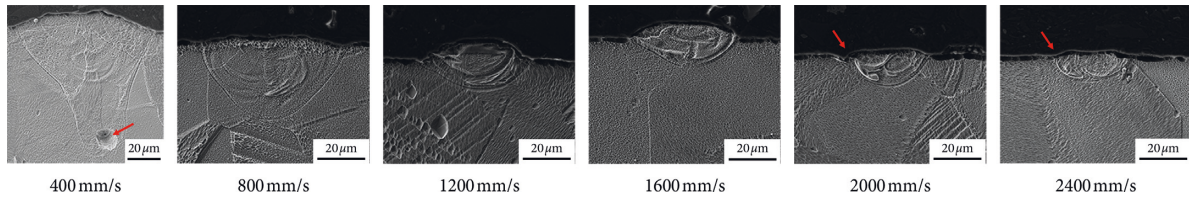
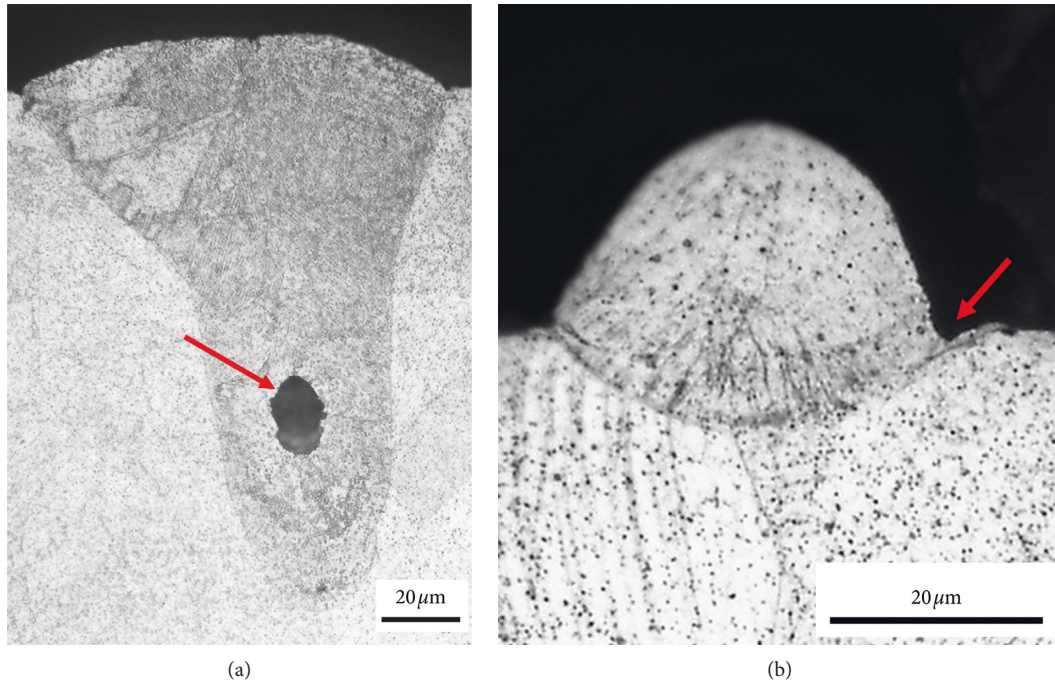FIGURE 8: SEM images of the cross section with different molten pool modes ($P = 60$ W).

(a)

(b)

FIGURE 9: Typical defects in the single tracks in micro-SLM: (a) keyhole pore ($P = 100$ W $v = 400$ mm/s) and (b) cavity at the edges ($P = 100$ W $v = 2800$ mm/s).
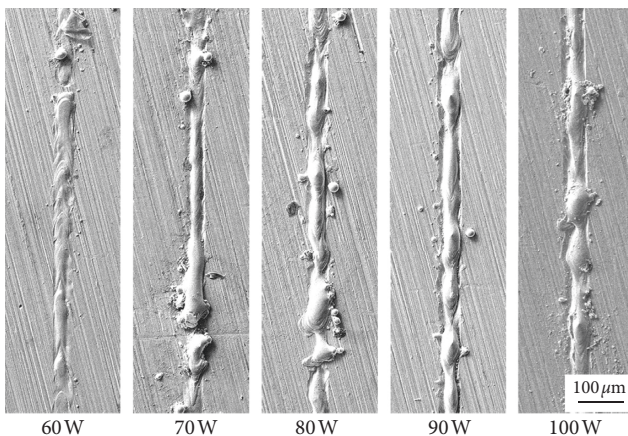

FIGURE 10: Evolution of edge cavity defect with changing laser powers ($v = 2800$ mm/s).

shows the SEM images of the surface of the single track with cavity. There is an obvious trace at the edges of the molten pool. Even some of the discontinuous tracks (60 W/70 W) also display the occurrence of the cavity. It has an adverse effect on the roughness of the surface perpendicular to the laser scanning direction. Besides, it is also detrimental for the liquid spreading of the following track during the multitrack fabrication.

Table 4 also highlights the process window for the single track without defects (red lines). The defect-free process window is inclusive of both the keyhole mode and conductive mode. In the conventional SLM process [23], a trail of voids can be found in the keyhole mode molten pool due to the collapse of a keyhole. Wei et al. [24] preferred the conductive-mode tracks in SLM because they are pore-free. Nevertheless, Yang et al. [9] reported that the keyhole mode can acquire better mechanical properties even though the conductive mode has a better formability. From their study, it was identified that keyhole mode can result in pore-free parts with the optimized process parameters. Therefore, it can be understood that the keyhole mode is not necessarily an undesirable mode in SLM, as observed from Table 4 for the micro-SLM as well. According to the results in Table 4, cavity at the edges is another defect that should be avoided. It emphasizes the fact that the conductive mode can also result in defects. Also, the continuity of the track is not the only criteria for the conductive mode to make it preferable. The best formability of the single track occurs at the

transition zone between the conductive mode and the keyhole mode.

4. Conclusion

Single track samples have been fabricated by different laser powers and scanning velocities in order to study the effect of process parameters on the formability, molten pool geometry, and the defects in micro-SLM. Following conclusions can be drawn from the results:

(1) The continuity of the track is determined by the laser power and scanning velocity. Fluid flow plays an important role. Once track is continuous and the fluid flow driving forces match the demand for the spreading of the molten pool, the surface roughness can be relatively low. The lowest surface roughness that can be achieved in this micro-SLM experiment is 1 μm.

(2) The geometry of the molten pool is directly determined by the laser power and scanning velocity. "Double-crest" surface occurs commonly because of the extremely small laser beam spot in the micro-SLM, which is different from the SLM process. Large recoil pressure gradient leads to formation of crests on both sides.

(3) The width, depth, and height of the molten pool have a close relationship with laser power and scanning velocity. The fluid spreading has effect on the height of the molten pool. The molten pool mode is also determined by the process parameters. A high laser power and low scanning velocity can lead to the keyhole mode of heat transfer.

(4) There are two typical defects in the single track which is significantly controlled by the process parameters. The keyhole pore only takes place in the keyhole mode molten pool because of the entrapped gas. The cavity at the edges takes place with higher laser power and scanning velocity, which is detrimental for the subsequent tracks during the 3D part fabrication. The best formability of the single track occurs at the transition zone between the conductive mode and the keyhole mode.

Data Availability

All data included in this study are available upon request by contacting the corresponding author.

Conflicts of Interest

The authors declare that there are no conflicts of interest regarding the publication of this paper.

Acknowledgments

References

[1] T. DebRoy, H. L. Wei, J. S. Zuback et al., "Additive manufacturing of metallic components - process, structure and properties," *Progress in Materials Science*, vol. 92, pp. 112–224, 2018.

[2] Y. Qin, A. Brockett, Y. Ma et al., "Micro-manufacturing: research, technology outcomes and development issues," *International Journal of Advanced Manufacturing Technology*, vol. 47, no. 9–12, pp. 821–837, 2009.

[3] R. Balasubramaniam and R. Shukla, "Micromanufacturing: a review—part I," *Proceedings of the Institution of Mechanical Engineers, Part B: Journal of Engineering Manufacture*, vol. 228, no. 9, pp. 973–994, 2014.

[4] Z. Hu, H. Zhu, X. Nie, C. Zhang, H. Zhang, and X. Zeng, "On the role of atmospheric oxygen into mechanical properties and fracture behavior of selective laser melted AlCu5MnCdVA," *Materials & Design*, vol. 150, pp. 18–27, 2018.

[5] U. S. Bertoli, A. J. Wolfer, M. J. Matthews, J. P. R. Delplanque, and J. M. Schoenung, "On the limitations of volumetric energy density as a design parameter for selective laser melting," *Materials & Design*, vol. 113, pp. 331–340, 2017.

[6] C. Kamath, B. El-dasher, G. F. Gallegos, W. E. King, and A. Sisto, "Density of additively-manufactured, 316L SS parts using laser powder-bed fusion at powers up to 400 W," *International Journal of Advanced Manufacturing Technology*, vol. 74, no. 1–4, pp. 65–78, 2014.

[7] J. Fischer, M. Kniepkamp, and E. Abele, "Micro laser melting: analyses of current potentials and restrictions for the additive manufacturing of micro structures," in *Proceedings of 25th Annual International Solid Freeform Fabrication Symposium 2014*, pp. 22–35, Darmstadt, Germany, 2014.

[8] I. Yadroitsev, P. Krakhmalev, I. Yadroitsava, S. Johansson, and I. Smurov, "Energy input effect on morphology and microstructure of selective laser melting single track from metallic powder," *Journal of Materials Processing Technology*, vol. 213, no. 4, pp. 606–613, 2013.

[9] J. Yang, J. Han, H. Yu et al., "Role of molten pool mode on formability, microstructure and mechanical properties of selective laser melted Ti-6Al-4V alloy," *Materials & Design*, vol. 110, pp. 558–570, 2016.

[10] X. Nie, H. Zhang, H. Zhu, Z. Hu, L. Ke, and X. Zeng, "Analysis of processing parameters and characteristics of selective laser melted high strength Al-Cu-Mg alloys: from single tracks to cubic samples," *Journal of Materials Processing Technology*, vol. 256, pp. 69–77, 2018.

[11] Y. Xiang, S. Zhang, Z. Wei et al., "Forming and defect analysis for single track scanning in selective laser melting of Ti6Al4V," *Applied Physics A*, vol. 124, p. 685, 2018.

[12] E. Abele and M. Kniepkamp, "Analysis and optimisation of vertical surface roughness in micro selective laser melting," *Surface Topography: Metrology and Properties*, vol. 3, article 034007, 2015.

[13] M. Kniepkamp, J. Fischer, and E. Abele, "Dimensional accuracy of small parts manufactured by micro selective laser melting," in *Proceedings of 26th Annual International Solid Freeform Fabrication Symposium 2016*, pp. 1530–1537, Darmstadt, Germany, 2016.

[14] N. T. Aboulkhair, I. Maskery, C. Tuck, I. Ashcroft, and N. M. Everitt, "On the formation of AlSi10Mg single tracks

and layers in selective laser melting: microstructure and nano-mechanical properties," *Journal of Materials Processing Technology*, vol. 230, pp. 88–98, 2016.

[15] Z. Hu, H. Zhu, C. Zhang, H. Zhang, T. Qi, and X. Zeng, "Contact angle evolution during selective laser melting," *Materials & Design*, vol. 139, pp. 304–313, 2018.

[16] G. Casalino, S. L. Campanelli, N. Contuzzi, and A. D. Ludovico, "Experimental investigation and statistical optimisation of the selective laser melting process of a maraging steel," *Optics & Laser Technology*, vol. 65, pp. 151–158, 2015.

[17] Z. Xiang, M. Yin, G. Dong, X. Mei, and G. Yin, "Modeling of the thermal physical process and study on the reliability of linear energy density for selective laser melting," *Results in Physics*, vol. 9, pp. 939–946, 2018.

[18] D. Dai and D. Gu, "Tailoring surface quality through mass and momentum transfer modeling using a volume of fluid method in selective laser melting of TiC/AlSi10Mg powder," *International Journal of Machine Tools and Manufacture*, vol. 88, pp. 95–107, 2015.

[19] V. Semak and A. Matsunawa, "The role of recoil pressure in energy balance during laser materials processing," *Journal of Physics D: Applied Physics*, vol. 30, pp. 2541–2552, 1999.

[20] S. A. Khairallah, A. T. Anderson, A. Rubenchik, and W. E. King, "Laser powder-bed fusion additive manufacturing: physics of complex melt flow and formation mechanisms of pores, spatter, and denudation zones," *Acta Materialia*, vol. 108, pp. 36–45, 2016.

[21] M. J. Matthews, G. Guss, S. A. Khairallah, A. M. Rubenchik, P. J. Depond, and W. E. King, "Denudation of metal powder layers in laser powder bed fusion processes," *Acta Materialia*, vol. 114, pp. 33–42, 2016.

[22] R. Fabbro, "Scaling laws for the laser welding process in keyhole mode," *Journal of Materials Processing Technology*, vol. 264, pp. 346–351, 2019.

[23] W. E. King, H. D. Barth, V. M. Castillo et al., "Observation of keyhole-mode laser melting in laser powder-bed fusion additive manufacturing," *Journal of Materials Processing Technology*, vol. 214, pp. 2915–2925, 2014.

[24] K. Wei, Z. Wang, and X. Zeng, "Preliminary investigation on selective laser melting of Ti-5Al-2.5Sn α-Ti alloy: from single tracks to bulk 3D components," *Journal of Materials Processing Technology*, vol. 244, pp. 73–85, 2017.

The Scientific World Journal

Journal of Applied Chemistry

Journal of Nanomaterials

Scientifica

International Journal of Polymer Science

Advances in Chemistry

Advances in Physical Chemistry

International Journal of Analytical Chemistry

Hindawi

Submit your manuscripts at
www.hindawi.com

Advances in Condensed Matter Physics

Journal of Chemistry

International Journal of Biomaterials

Advances in High Energy Physics

Journal of Engineering

Journal of Nanotechnology

International Journal of Corrosion

Journal of Materials

BioMed Research International

Advances in Tribology

Advances in Materials Science and Engineering